Topics in Catalysis (2019) 62:524–534
https://doi.org/10.1007/s11244-019-01148-3

ORIGINAL PAPER

CO_2 Methanation in the Presence of Ce-Promoted Alumina Supported Nickel Catalysts: H_2S Deactivation Studies

Wojciech Gac[1] · Witold Zawadzki[1] · Marek Rotko[1] · Grzegorz Słowik[1] · Magdalena Greluk[1]

Published online: 28 February 2019
© The Author(s) 2019

Abstract
The performance of alumina supported unpromoted and cerium promoted nickel catalysts in CO_2 methanation reaction was investigated. It was found that the activity of catalysts in CO_2 methanation reaction at low reaction temperatures can be improved by the increase in nickel loading and introduction of cerium promoter. The catalysts showed high resistance for sintering and coking at high reaction temperatures. A few stages of catalysts deactivation by H_2S in the methanation reaction carried out at 475 °C with the time on stream were identified. It was found that an introduction of H_2S to the stream (8 ppm) did not induce rapid decrease of activity. Slight and then strong drop of CO_2 conversion and simultaneously the loss of methane selectivity was observed after specific time, depending on the catalysts composition. Deactivation of catalysts was related to the nickel content and the presence of cerium. X-ray diffraction studies indicated small changes of crystallite size with the time on stream. Raman spectroscopy studies pointed out that deactivation of catalysts was not connected with formation of carbon deposits. An in-situ Diffuse Reflectance Infrared Fourier Transform Spectroscopy studies showed that exposition of catalysts to the reaction mixture containing the traces of H_2S led to the blocking of nickel active sites responsible for CO_2 and H_2 activation and successive transformation to carbonyl and formate species.

Keywords Nickel catalyst · Alumina · Ce promoter · CO_2 methanation · H_2S poisoning

1 Introduction

The increase in the demand for energy carriers and chemical products in the last decades, connected with an increase in population growth and industrial development has brought significant environmental threats, including over-exploitation of natural resources, massive consumption of fossil fuels and greenhouse gas emission, unprecedented in the history of civilization [1, 2]. More and more attention is paid to the capture and utilization of carbon dioxide formed during combustion of fossil fuels, transformation of wastes and conversion of biomass, e.g. for production of energy carriers and valuable chemicals, such as methane, methanol, dimethyl ether, polymers. An application of biomass for production of energy and valuable chemical compounds has found wide interest for many years [3–6]. Biomass is characterized by variability of chemical composition, and may contain both the complex compounds of carbon, hydrogen and oxygen, as well as some compounds of sulfur, nitrogen or phosphorus. The composition of biogas depends on the production conditions and the type of raw materials used [7]. The main components of biogas are methane and carbon dioxide. The heating value of biogas can be increased by removal of carbon dioxide. Methanation reaction is regarded as an alternative solution for the (bio)-CO_2 utilization.

$$CO_2 + 4H_2 \rightarrow CH_4 + 2H_2O \quad \Delta H^0_{298K} = -165 \text{ kJ mol}^{-1} \tag{1}$$

The advantage of such idea is the possibility of simultaneous utilization of hydrogen, produced with the participation of renewable energy. Methanation of carbon dioxide (Sabatier reaction) has been introduced to the industry at the beginning of the last century [8]. Initially, studies were concerned on the improvement of fuel gasification processes for heat production. In turn, methanation of carbon oxide is used in the industrial scale for purification of synthesis gas in the production of ammonia. Nowadays, the interest of CO_2 utilization results mainly from the environmental issues, reduction

✉ Wojciech Gac
wojciech.gac@umcs.lublin.pl

[1] Department of Chemical Technology, Faculty of Chemistry, Maria Curie-Sklodowska University, 3 M. Curie-Skłodowska Sq, 20-031 Lublin, Poland

in the greenhouse effect caused by the consumption of fossil fuels. The development of active, selective and durable bio-CO_2 methanation catalysts is a challenge; the catalysts should show high activity, selectivity, resistance for sintering, coking and poisoning. Nickel catalysts have been widely studied for hydrogenation of carbon oxides. High dispersion has often been achieved by the application of the supports of high specific surface area or particular structure and porosity, including γ-Al_2O_3 [9–14], nanostructured silica supports [15, 16], zeolites [17], CeO_2 [18, 19], $Ce_xZr_{1-x}O_2$ [20–22], ZrO_2–Al_2O_3 [23], hydrotalcites [24–27], $MgAl_2O_4$ spinels [28]. Nickel dispersion has been also improved by the use of suitable promoters and modifiers, e.g. Ce [29–32], La [33–37], Mo [38], W [39], Mn [40], Fe [41–43].

Hydrogen sulfide (H_2S) is found to be the most unfavorable component of biogas. Its presence may strongly hinder the potential application of biogas for production of energy and chemical bio-products. H_2S is a colorless gas, heavier than air with characteristic smell. It dissolves well in water. It is a toxic gas, fortunately the hydrogen sulfide odor threshold is very low (0.18 mg/m^3). H_2S is crucial for biogas plants operation, hence some of them use desulfurization and biogas drying units. Several concepts of catalytic methanation of carbon dioxide contained in biogas can be distinguished. The first concept assumes the hydrogenation of bio-CO_2 without purifying the stream from sulfur compounds, but at their concentration at the level that ensures the operation of catalysts in the form of sulfides. Available literature data in carbon oxides hydrogenation over such catalysts are very scant. Mostly, studies have been focused on the hydrogenation reaction of carbon monoxide, e.g. contained in the synthesis gas produced by gasification of sulfated coal. Typical representatives of this group are molybdenum based catalysts [44–46]. The processes of deactivation of sulfide catalysts are mainly related to the structural changes of the corresponding sulfides. The second concept assumes complete removal of sulfur-containing compounds from the biogas or bio-CO_2 stream prior to the methanation reaction. Carbon dioxide in the purified waste stream or directly in biogas would be then converted over noble or non-noble metal catalysts. Numerous studies were focused on the influence of sulfur compounds on the performance of catalysts in natural gas or biogas reforming reactions [47]. However, there is very little information on the effects of sulfur compounds on the methanation of CO_2 in biogas stream.

The aim of the studies was determination of the activity and durability of cerium promoted alumina supported nickel catalysts in CO_2 methanation reaction in H_2S free and contaminated streams.

2 Experimental

2.1 Preparation of Catalysts

Nickel catalysts were prepared by the impregnation method using γ-Al_2O_3 as support (Alfa Aesar). Finally grinded support (5 g) was introduced to the aqueous solution obtained by the dissolution of the suitable amounts of nickel nitrate hexahydrate ($Ni(NO_3)_2 \cdot 6H_2O$, p.a., Sigma Aldrich) and citric acid (Sigma Aldrich) in 300 mL of deionized water. Molar ratio of nickel nitrate to citric acid was maintained at 1:1. The mixture was heated at ~ 90 °C to evaporate water while stirring. Samples were dried overnight at 120 °C, and then calcined at 400 °C for 2 h to decompose metal precursors. Similar procedures were used for synthesis of ceria promoted catalysts. In this case, an aqueous solution was prepared using nickel nitrate, cerium nitrate hexahydrate ($Ce(NO_3)_3 \cdot 6H_2O$, p.a., Sigma Aldrich) and citric acid, keeping molar ratio of metal salts to citric acid 1:1.

2.2 Characterization of Catalysts

X-ray fluorescence method with ED-XRF Canberra-Packard 1510 spectrometer was used for determination of nickel and cerium content in the catalysts. Surface properties and porosity of catalysts were determined from nitrogen adsorption/desorption measurements obtained volumetrically at − 196 °C by means of ASAP 2405N analyzer (Micromeritics Instr. Corp.). The standard Brunauer–Emmett–Teller (BET) method was used for determination of the specific surface area (S_{BET}). Pore size distribution and mean pore were estimated from the desorption branch of isotherms by the dimeter Barret–Joyner–Halenda (BJH) method. Phase composition of catalysts after reduction in hydrogen (600 °C for 2 h) and spent catalysts after durability tests was determined by the X-ray diffraction method (XRD) using Empyrean (PANalytical) diffractometer with Cu Kα radiation ($\lambda = 1.5418$ Å). Mean nickel crystallite size (d_{Ni}^{XRD}) was estimated by the application of Rietveld method implemented in the HighScore Plus software [48]. An active surface area of catalysts (S_a) was calculated from the static volumetric chemisorption method using ASAP 2020C apparatus (Micromeritics Inst. Corp.) under assumption of the chemisorption stoichiometry of H:Ni = 1:1 and 0.0649 nm^2 surface area occupied by single hydrogen atom [48]. The catalysts prior to the chemisorption of hydrogen (at 35 °C) were reduced at 600 °C for 2 h and evacuated under the vacuum of 3.8×10^{-7} Pa. Hydrogen chemisorption data were applied for supplementary estimation of mean nickel crystallite size (d_{Ni}^{Ch}) under assumption of the spherical shape of crystallites:

$d_{Ni}^{Ch} = \frac{6\times10^3}{\delta_{Ni}\times S_{Ni}}$, where:, δ_{Ni}—density of nickel (g/cm^3), S_{Ni}—surface area of nickel in catalysts (m^2/g$_{Ni}$).

Scanning electron microscopy studies of the catalysts after durability tests were performed by the application of Quanta 3D FEG microscope (FEI), equipped with Field Emission Gun. The catalysts prior to the durability tests and after reaction were studied by means of Raman spectroscopy using in Via Reflex spectrometer (Renishaw) equipped with 514 nm laser. An in-situ CO_2 methanation reaction studies were performed by the application of Diffuse Reflectance Infrared Fourier-Transform spectroscopy (DRIFTS) with automated gas distribution system (Medson), FT-IR spectrometer (Nicolet 6700, Thermo Scientific) with LN_2 cooled MCTA detector and Praying Mantis High-temperature Reaction Chamber (Harrick) with ZnSe windows [49]. The background signal was determined by the use of KBr. The spectra were recorded in the methanation reaction performed over activated catalysts and after durability tests. In the first case, the samples were reduced at 600 °C for 2 h, then the temperature was decreased to 100 °C and the mixture of CO_2 (10 mL/min), H_2 (40 mL/min) and Ar (5 mL/min) was introduced to the reaction chamber. DRIFT spectra were recorded at selected temperatures from 100 to 400 °C in the wavenumber range of 650–4000 cm^{-1} and the resolution of 4 cm^{-1}. The samples of spent catalysts after durability tests and passivation at room temperature, were taken from the reactor and transferred to the DRIFTS reaction chamber. Samples were reduced in the stream of hydrogen at 100 °C to perform possible depassivation. Next DRIFTS spectra were recorded at selected temperatures as described above.

Catalysts activity tests in CO_2 methanation reaction were carried out in the reaction system (PID Eng & Tech) operated under the pressure $p = 1.9\times10^5$ Pa (~ 1.9 bar) by the application of a fixed-bed continuous-flow quartz reactor in a similar way as described in Ref [48]. The sample of catalyst (0.2 g) was mixed with quartz scraps. Reduction was performed at 600 °C for 2 h in the flow of hydrogen. CO_2 methanation reaction was carried out in the mixture of pure components H_2 (61.6 vol%), CO_2 (15.4 vol%) and Ar (23 vol% Ar) with the total flow rate of 100 mL/min, weight hourly space velocity referenced to CO_2 in the feed (WHSV) 4.6 $L_{CO_2}h^{-1}g^{-1}$, and contact time equal to 0.21 h g $L_{CO_2}^{-1}$. The analysis of CO_2 methanation reaction product was carried out by the customized Bruker's Rapid RGA Analyzer based on a 450-GC. The carbon dioxide conversion (X_{CO_2}), methane and carbon monoxide selectivity (S_{CH_4}, S_{CO}) were calculated using the following equations: $X_{CO_2} = \frac{C_{CO_2}^{in} - C_{CO_2}^{out}}{C_{CO_2}^{in}} \times 100\%$, $S_{CH_4} = \frac{C_{CH_4}}{C_{CH_4}+C_{CO}} \times 100\%, S_{CO} = \frac{C_{CO}}{C_{CH_4}+C_{CO}} \times 100\%$, where $C_{CO_2}^{in}$—is the molar concentration of CO_2 in the reaction mixture, $C_{CO_2}^{out}$—is the molar concentration of CO_2 in the post-reaction mixture, C_{CH_4}, C_{CO}—the molar concentrations of the CH_4 and CO in the post-reaction mixture.

Fully customized system for long-term tests studies was used. Durability tests were performed in the similar conditions as activity tests, described above. The system consisted of mass flow controllers, suitable valves, fixed-bed continuous-flow quartz reactor, electric furnace, water trap, and was coupled to fast Micro-GC analyzer (CP-4900, Bruker). The analysis of reaction products was automatically performed every 30 min. Conversion of CO_2 and selectivity to CH_4 and CO were calculated from the suitable equations, stated above. The catalysts were initially reduced at 600 °C for 2 h, then the temperature was decreased to 475 °C and the reaction was performed in the stream of CO_2, H_2 and Ar mixture ($H_2/CO_2 = 4$) for 20 h. Next, the composition of the reaction mixture was changed, replacing pure hydrogen by the premixed H_2–H_2S mixture. The content of H_2S in the reaction mixture was equal 8 ppm. The reaction tests were carried out for several hours, until the loss of initial activity (usually 70–80 h). The catalysts after the tests were cooled down in the flow of inert gas to the room temperature and gently passivated.

3 Results and Discussion

3.1 Properties of Catalysts Determined Prior to the CO_2 Methanation Reaction

Two groups of catalysts containing ca. 20 and 40 wt% Ni were studied. The Table 1 presents composition of

Table 1 Nickel and cerium content, specific surface area (S_{BET}), mean pore diameter (D_{BJH}) and mean nickel crystallite size estimated from XRD (d_{Ni}^{XRD}) and hydrogen chemisorption (d_{Ni}^{Ch}) studies, and active surface area (S_a) of catalysts

Catalyst	Composition (wt. %)		S_{BET} (m^2/g)	D_{BJH} (nm)	d_{Ni}^{XRD} (nm)	d_{Ni}^{Ch} (nm)	S_a (m^2/g)
	Ni	Ce					
Al_2O_3	–	–	251.7	12.2	–	–	–
Ni20–Al_2O_3	19.2	–	236.7	8.2	4.2	10.3	12.5
Ni40–Al_2O_3	36.9	–	260.5	6.1	6.3	13.7	18.1
Ni20–Ce5–Al_2O_3	20.7	5.3	242.7	7.6	3.5	9.9	14.1
Ni40–Ce5–Al_2O_3	39.2	5.5	228.9	7.7	6.4	13.5	19.6

catalysts. The catalysts were modified by the introduction of Ce promoter (ca. 5 wt%). The specific surface area of alumina support was relatively large, and equal to 251.7 m^2/g, while mean pore diameter was in the mesoporous region, equal to 12.2 nm. Surface properties and porosity of catalyst are not strongly different from that of the support. The specific surface area of obtained catalysts was in the range of 230–260 m^2/g, while mean pore dimeter was irregularly varied in the range of 7–8 nm (Table 1). Fig. 1 shows X-ray diffraction curves of reduced catalysts. The catalysts prior to the reaction were activated in hydrogen at 600 °C for 2 h. Broad reflections of alumina and metallic nickel phases point out the presence of small nickel crystallites. Therefore, the calculated nickel crystallite size (d_{Ni}^{XRD}), despite the use of advanced Rietveld method, may contain some inaccuracies. Mean nickel crystallite size in Ni20–Al_2O_3 catalyst is equal 4.2 nm. An increase of nickel content to ca. 40 wt% leads to the slight increase of nickel crystallite size to $d_{Ni}^{XRD} = 6.3$ nm (Table 1). An introduction of cerium drives to the slight changes of mean nickel crystallite size to 3.5 and 6.4 nm for Ni20–Ce5–Al_2O_3 and Ni40–Ce5–Al_2O_3 catalyst, respectively. The lack of reflection of cerium oxide phases indicates their high dispersion.

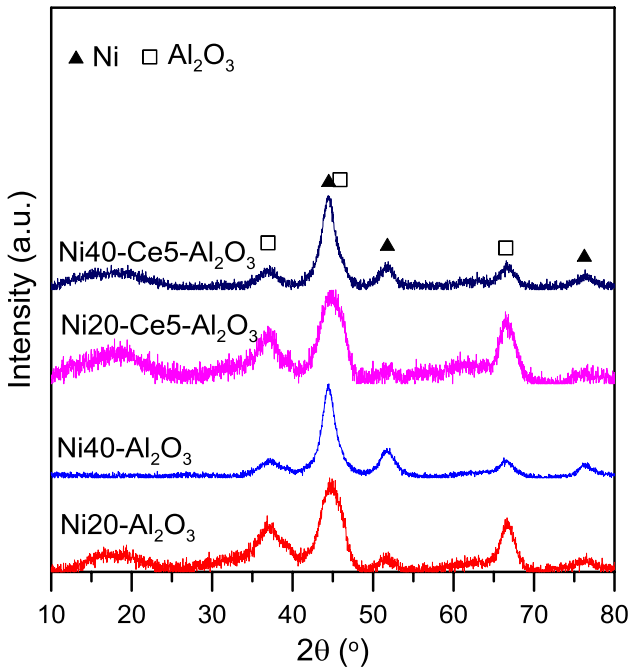

Fig. 1 X-ray diffraction curves of catalysts after reduction at 600 °C

The catalysts show relatively large active surface area, strictly connected to the presence of the small nickel crystallites. An increase of nickel content in the unpromoted catalysts from ca. 20 to 40 wt% leads to the increase of the active surface area from 12.5 to 18.1 m^2/g. The increase of the active surface area of the catalysts is also observed after introduction of Ce promoter. The active surface area increases to 14.1 and 19.6 m^2/g for Ni20–Ce5–Al_2O_3 and Ni40–Ce5–Al_2O_3 catalyst, respectively. It is found that mean nickel crystallite size determined on the basis of chemisorption data (assuming the spherical shape of particles and that all surface sites are accessible for hydrogen atoms) is greater for corresponding catalysts than that estimated from XRD studies. Such discrepancy may result from limited accessibility of surface sites and partial coverage of nickel crystallites by the support.

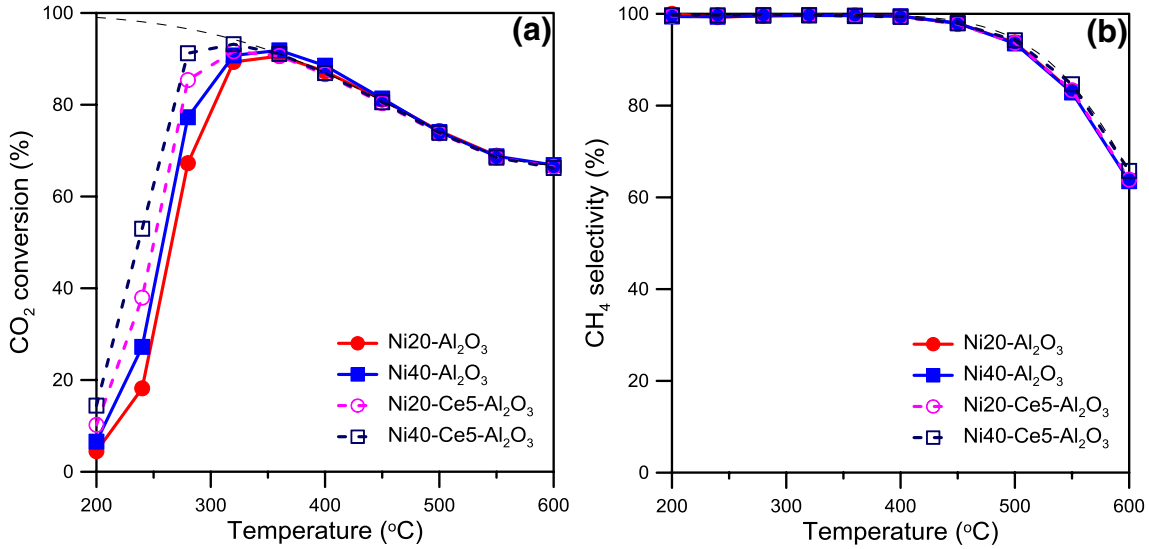

Fig. 2 (**a**) CO_2 conversion at selected temperatures, (**b**) selectivity of catalysts to methane

3.2 Methanation of Carbon Dioxide

Activity studies of CO_2 methanation reaction performed at different temperatures over unpromoted and promoted nickel alumina supported catalysts are presented in the Fig. 2. Carbon dioxide conversion increases from ca. 5 to 90% with an increase in reaction temperature from 200 to 350 °C. Above this temperature CO_2 conversion decreases in accordance to the thermodynamic limits [50]. An increase of nickel loading from ca. 20 to 40 wt% drives to the increase in CO_2 conversion at low reaction temperatures (200–350 °C). This effect is well visible in the range of 240–320 °C. An introduction of cerium promoter to the alumina supported catalyst containing ca. 20 wt% Ni result in the increase of CO_2 conversion at low reaction temperatures. Similar improvement of catalytic performance at low reaction temperatures is observed for Ce promoted catalyst with higher Ni content (Ni40–Ce5–Al_2O_3). It is found, that carbon monoxide formation is favored at higher temperatures. As a consequence, CH_4 selectivity decreases with an increase in reaction temperature. The catalysts show high selectivity to methane at low reaction temperatures (200–350 °C). However, CH_4 selectivity decreases from ~ 100% to ca. 60% when the reaction temperature is increased from 350 to 600 °C. The selectivity of catalysts is slightly changed after introduction of cerium. The observed changes of the activity of promoted catalysts are consistent with recently published data [32–36]. An increased activity of Ce and La promoted nickel catalysts has been often attributed

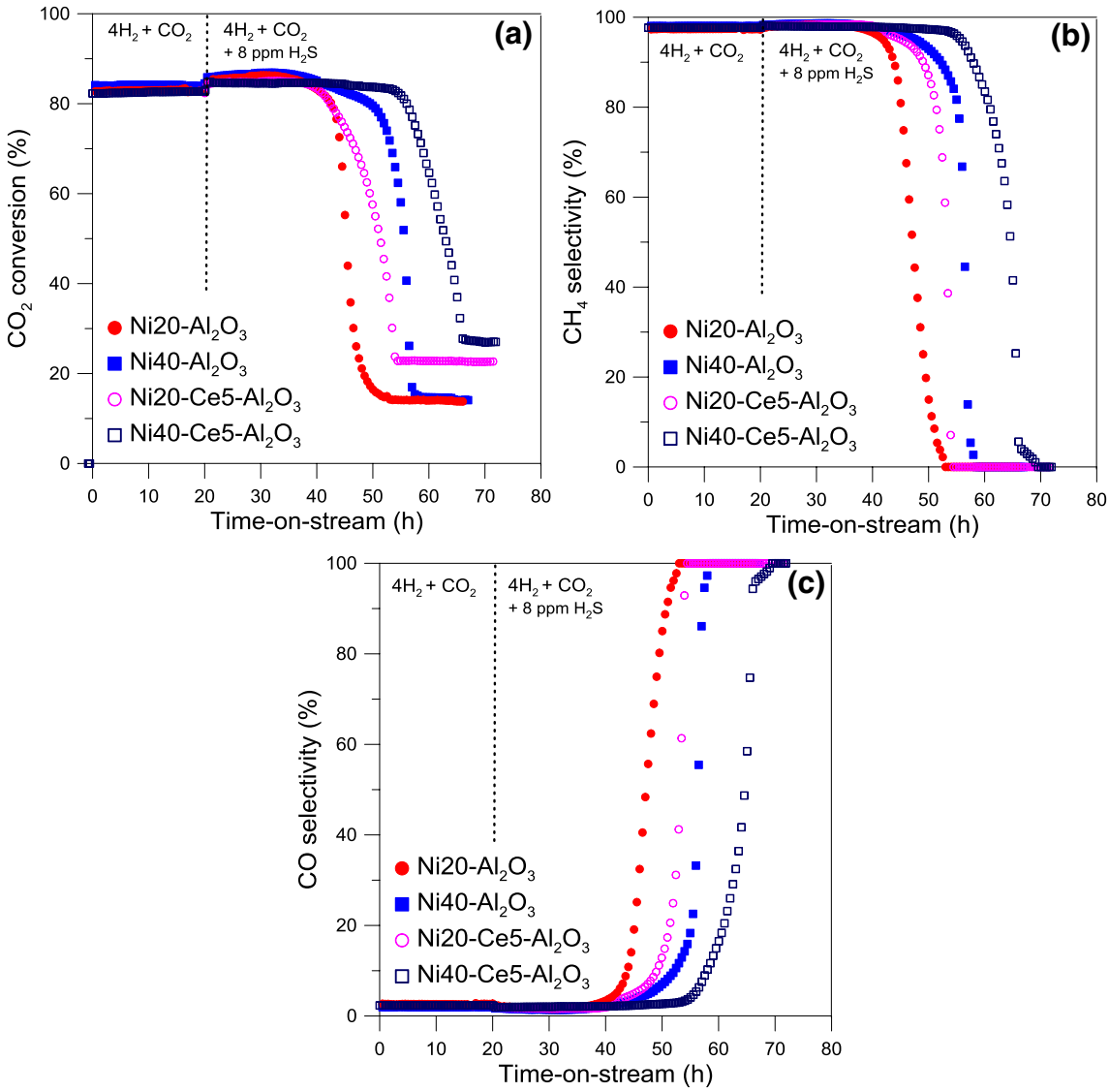

Fig. 3 Durability tests of catalysts in the reaction performed at 475 °C in the presence of CO_2 and H_2 components and after introduction of 8 ppm of H_2S; (**a**) CO_2 conversion, (**b**) CH_4 selectivity, (**c**) CO selectivity

in the literature to the improved nickel dispersion and changes of the acid-base properties of catalysts [32–36].

Figure 3 shows the results of durability studies of catalysts in CO_2 methanation reaction performed at 475 °C. The catalytic tests carried out in CO_2–H_2 reaction mixture at such relatively high reaction temperature evidenced no deactivation trends for catalysts over 20 h time on stream. CO_2 conversion and CH_4 selectivity has found to be high and stable for 20 h on stream. Such effects indicate high resistance of catalysts for sintering and coking. The catalysts after 20 h of the operation on pure components CO_2 and H_2 were subjected to the mixture containing traces of H_2S (8 ppm). Three stages of CO_2 conversion changes can be found. In the first period, only slight decline is visible. Next, a rapid drop of CO_2 conversion is observed, and finally very low conversion is detectable. Initially relatively high CO_2 conversion and selectivity to methane is observed for Ni20–Al_2O_3 catalyst. It shows no signs of deactivation for about 20 h after introduction of H_2S. Slight drop of CO_2 conversion and decrease of selectivity to methane is visible after suitable initial period. In the next stage, the decrease of CO_2 conversion becomes evident. Conversion of CO_2 approaches low level in the final stage, while the selectivity to methane falls completely to zero and carbon monoxide becomes the main reaction product. It is interesting that the effects of the decrease of CO_2 conversion and selectivity changes occur almost simultaneously. Similar effects are observed for the catalyst of higher nickel loading. The initial period of high activity after introduction of H_2S in the case of Ni40–Al_2O_3 catalyst is longer. A slight drop of CO_2 conversion after about 20 h time on stream over the next 10 h is more visible than in the presence of catalyst of lower nickel loading. The next stage - fast deactivation occurs almost with the same rate. Consequently, CO_2 conversion for Ni40–Al_2O_3 catalyst declines to the same low level as for Ni20–Al_2O_3 (close to 10%).

Deactivation of cerium promoted catalysts occurs through similar stages. Initial period of deactivation of Ni20–Ce5–Al_2O_3 catalyst is almost the same as for Ni20–Al_2O_3. However, the next stage of deactivation is much longer and the slope of the deactivation curve is smaller. Similar deactivation stages are visible for Ni40–Ce5–Al_2O_3 catalyst, but much longer initial period can be detected. Consequently, Ni40–Ce5–Al_2O_3 catalyst demonstrates the best resistance for poisoning. Note, that the final level of CO_2 conversion is higher for both catalysts containing cerium in comparison to unpromoted ones (ca. 20 and 25% for Ni20–Ce5–Al_2O_3 and Ni40–Ce5–Al_2O_3 catalysts, respectively).

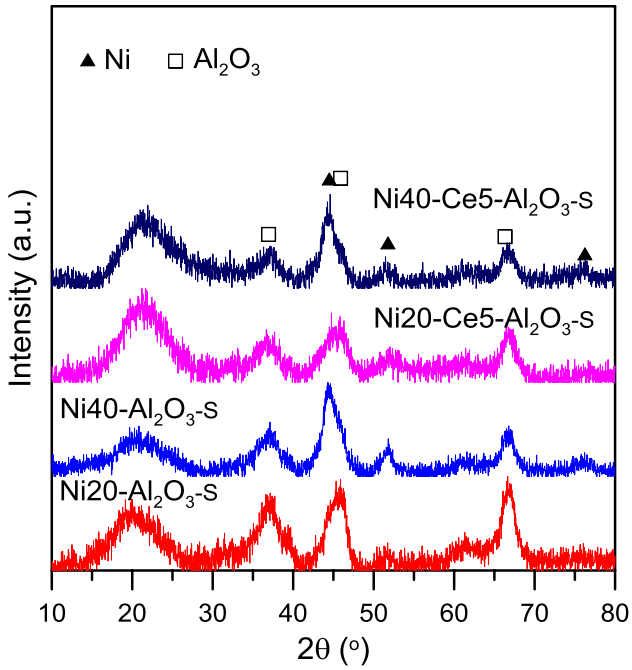

Fig. 4 X-ray diffraction curves of spent catalysts after durability tests performed in the presence of H_2S. Spent catalysts were denoted adding "S" to the name

3.3 Properties of Spent Catalysts

Deactivation of catalysts may result from several reasons, including sintering, coking and poisoning with H_2S. XRD curves of spent catalysts after durability tests, transferred from the reactor are presented in the Fig. 4. The names of the relevant catalysts studied after deactivation have been changed by adding the letter "*S*". X-ray diffraction patterns of catalysts prior to the reaction and after durability tests are very similar. Wide reflections in the low theta angles result from the presence of the traces of quartz grains used for dilution of the catalysts samples. The shape of XRD peaks of catalysts before and after the tests is very similar. Broad reflections of alumina and metallic nickel phases are well visible. The size of nickel crystallites in corresponding catalysts is similar. Mean size of nickel crystallites in the case of Ni20–Al_2O_3 and Ni40–Al_2O_3 catalysts is equal to 4.6 and 6.9 nm, respectively. While mean size of nickel crystallites in the promoted catalysts is equal to 5.6 and 6.3 nm for Ni20–Ce5–Al_2O_3 and Ni40–Ce5–Al_2O_3. Therefore, it can be concluded, that sintering of catalysts is not a factor responsible for pronounced deactivation of catalysts and drop of selectivity to methane.

Formation of different types of carbon deposits on the surface of catalysts has been often observed in numerous reactions, such as steam and dry reforming or cracking of organic compounds. Carbon deposits have been often easily identified in the catalysts on the basis of X-ray diffraction,

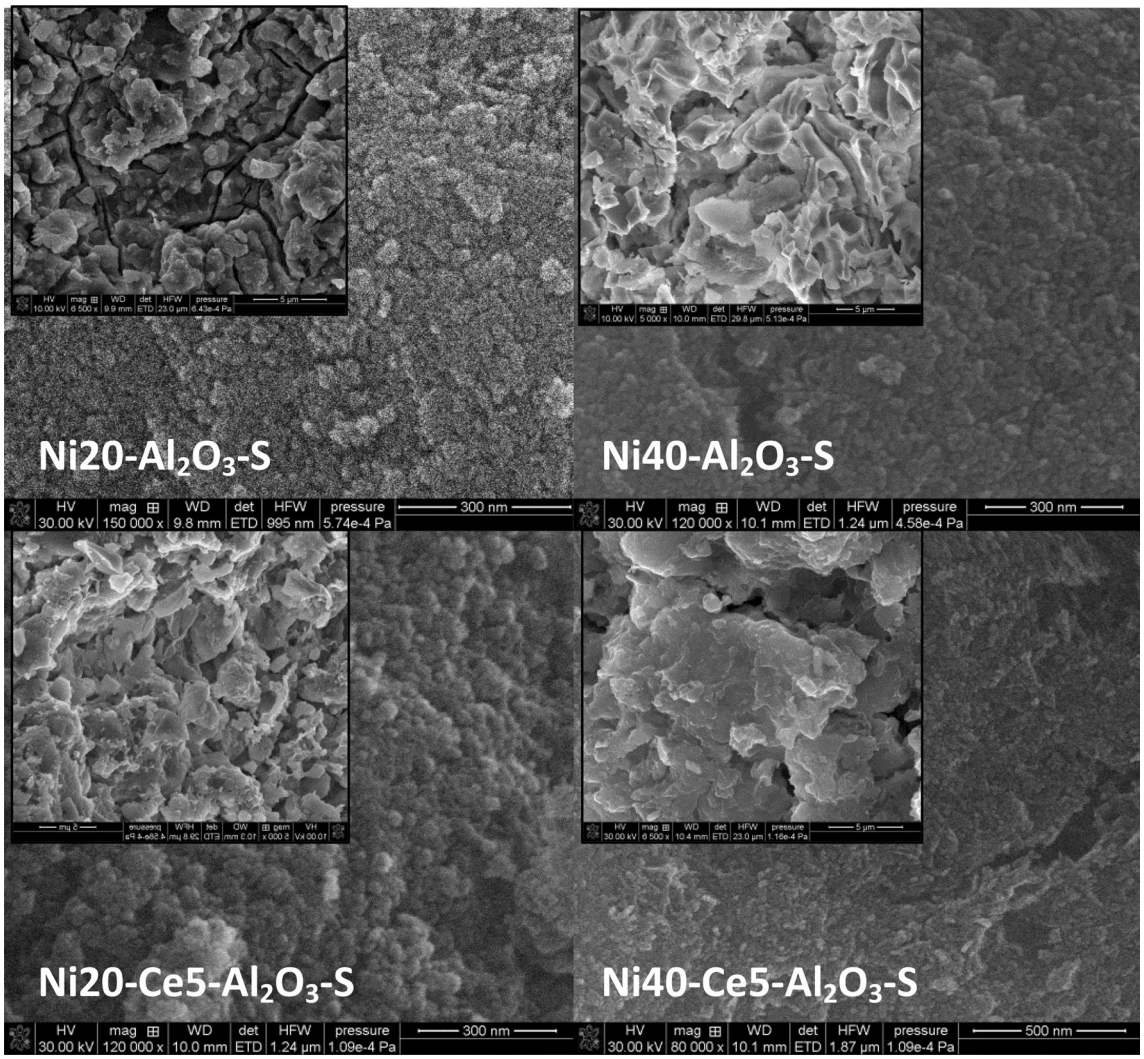

Fig. 5 SEM images of spent catalysts

microscopic studies and Raman spectroscopy. However, the distinct XRD reflection peaks of carbon are not observed on the curves of catalysts after deactivation. Hence, the presence of ordered carbonaceous deposits can be also excluded. Figure 5 shows SEM images of deactivated catalysts after durability tests. It is difficult to find any forms of carbonaceous deposits on the catalysts, such as carbon fibers or encapsulating carbons. However, the presence of some disordered surface forms can't be completely ruled out.

Figure 6 shows Raman spectra of catalysts recorded before and after durability tests in the presence of H_2S. Typical vibration bands of carbonaceous structures, usually occurred in the range of 1100–1700 cm^{-1} are not visible [49, 51–53]. Weak shoulder in the range of 400–500 cm^{-1} can be attributed to the vibration bands connected with the presence of CeO_x species. However due to the weak intensity, resulted from the small amounts of Ce it is difficult to determine the nature of oxides and/or their changes during the reaction. Hence, one can assume that the main reason of catalysts deactivation is poisoning of the catalytically active surface sites by sulfur. In turn, typical Raman vibrations of pure sulfur, sulfur organic compounds with C–S, C–H groups, as well as vibrations of NiS_x phases are also not visible, which may indicate formation of strongly dispersed sulfur surface species [54]. Hydrogen sulfide reaching the surface of the metal catalyst is dissociatively adsorbed, forming surface nickel sulfides, in accordance to the general reaction equation: $H_2S + xNi \rightarrow Ni_xS + H_2$. Surface nickel sulfides show high stability, even higher than bulk sulfides [55–57]. Their stability decreases with the temperature increase. H_2S chemisorption is an exothermic process, therefore the adsorption equilibrium depends on the temperature. However, adsorption of sulfur can be regarded as irreversible process at low temperatures. The adsorbed sulfur atoms at low surface coverages may cause distortion of the energetic state of the surface nickel atoms and introduce geometric hindrances,

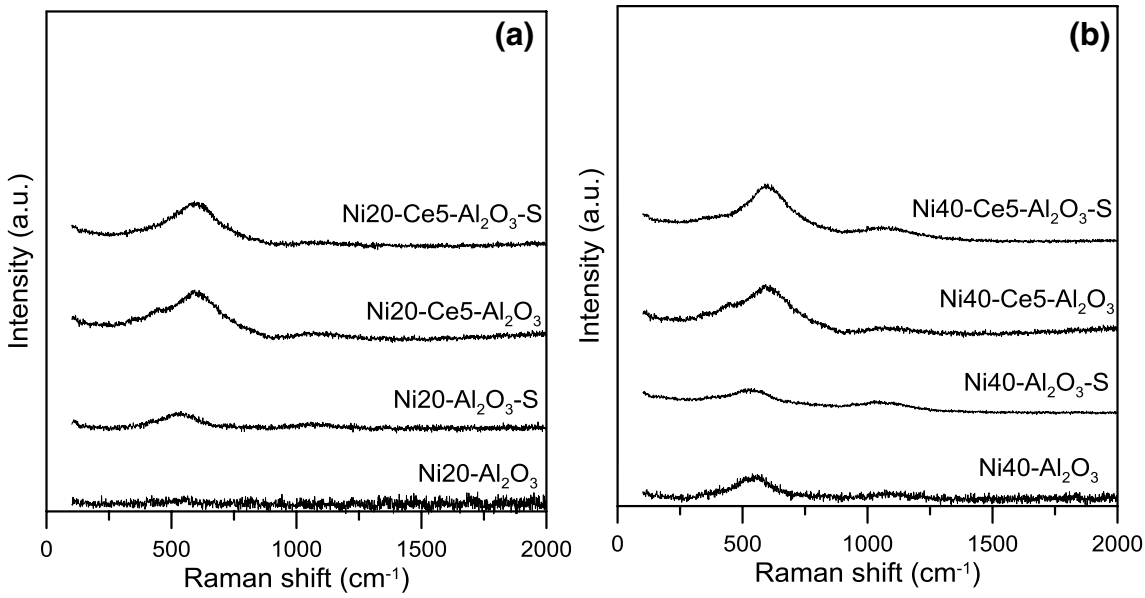

Fig. 6 Raman spectroscopy spectra of catalysts containing 20 wt% Ni (**a**) and 40 wt% Ni (**b**) after reduction at 600 °C and spent catalysts after durability tests performed in the presence of H_2S

whereas mainly geometric disturbances can be present at high coverages [58]. DFT calculations presented in the literature, show that sulfur atoms can be preferentially located on the crystal lattice defects, mainly Ni (211) sites, affecting processes related to methane conversion [58]. Literature data indicated that the local distribution of surface sulfur atoms depends on the coverage and type of planes; e.g. $p(2\times2)$ type structure was proposed for Ni (100) planes under low coverages $S/Ni_s < 0.25$, which is transformed to $c(2\times2)$ type on higher coverages $0.25 < S/Ni_s < 0.5$. It was argued that complete sulfur saturation of Ni(100) planes occurs at $S/Ni_s = 0.50$, but saturation for other planes may occurs at different S/Ni_s values, from 0.7 to 1.09 [58].

Figure 7 shows DRIFTS spectra recorded during in-situ CO_2 methanation reaction over catalysts subjected to the activation procedure in pure hydrogen at 600 °C (dashed lines) and over the spent catalysts transferred from the reactor after durability test in the presence of H_2S (solid lines). In the second case, the samples were pre-reduced in-situ at low temperature (100 °C) before spectra recording in the CO_2–H_2 reaction mixture. The dot lines represent spectra recorded over alumina support in the methanation reaction in the mixture of H_2–CO_2 at suitable temperatures. The support was also pre-reduced at 600 °C. DRIFTS spectra presented in the Fig. 7a in the range 1700–2200 cm^{-1} reveal characteristic vibrations of carbonyl groups on the surface of Ni20–Al_2O_3 catalysts [59–61]. The presence of vibration bands on the spectra recorded at 100 °C, shifted towards lower wavenumber values with respect to the ν(CO) in gas phases, indicates formation of carbonyl species in the initial step of CO_2 methanation reaction, which are located on the surface nickel sites (Ni^0). Distinct vibration bands, visible in the different regions can be ascribed to the differently coordinated species, i.e. linear carbonyls (located on top nickel sites ~ 1980–2100 cm^{-1}), twofold bridged carbonyls (1870–1980 cm^{-1}) and threefold bridged carbonyls on hollow sites (ca. 1780–1900 cm^{-1}) [59, 61]. Carbonyl groups are not visible on the spectra recorded during reaction performed in the presence of alumina. Similar vibration bands are not observed on the spectra recorded during in-situ methanation reaction over spent catalysts taken from the catalytic reactor after durability tests in the presence of H_2S. Such effects indicate, that the initial step of methanation reaction, connected with the transformation of CO_2 to CO on the surface of nickel is hindered in the deactivated catalysts due to the blockage of the active sites.

DRIFTS spectra recorded in the reaction performed at higher temperatures over active catalyst reveal changes of the contribution of differently coordinated carbonyl groups and gradual decrease of their intensity [62]. The vibration bands of carbonyl groups are not detectable on the spectra recorded over deactivated catalyst at high reaction temperatures in the CO_2 methanation reaction. We have also not observed such vibration bands after subsequent cooling down the catalyst to the low temperatures. Carbonyl vibrations bands are also not visible on the spectra of bare alumina at higher temperatures.

Figure 7b shows the spectra recorded for Ni20–Ce5–Al_2O_3 catalysts. One can see slight differences in the position and intensity of vibration bands of corresponding carbonyl groups. There is a slight relative increase in the intensity of bridged carbonyls and their shift towards higher wavenumbers in comparison to unpromoted catalyst on the

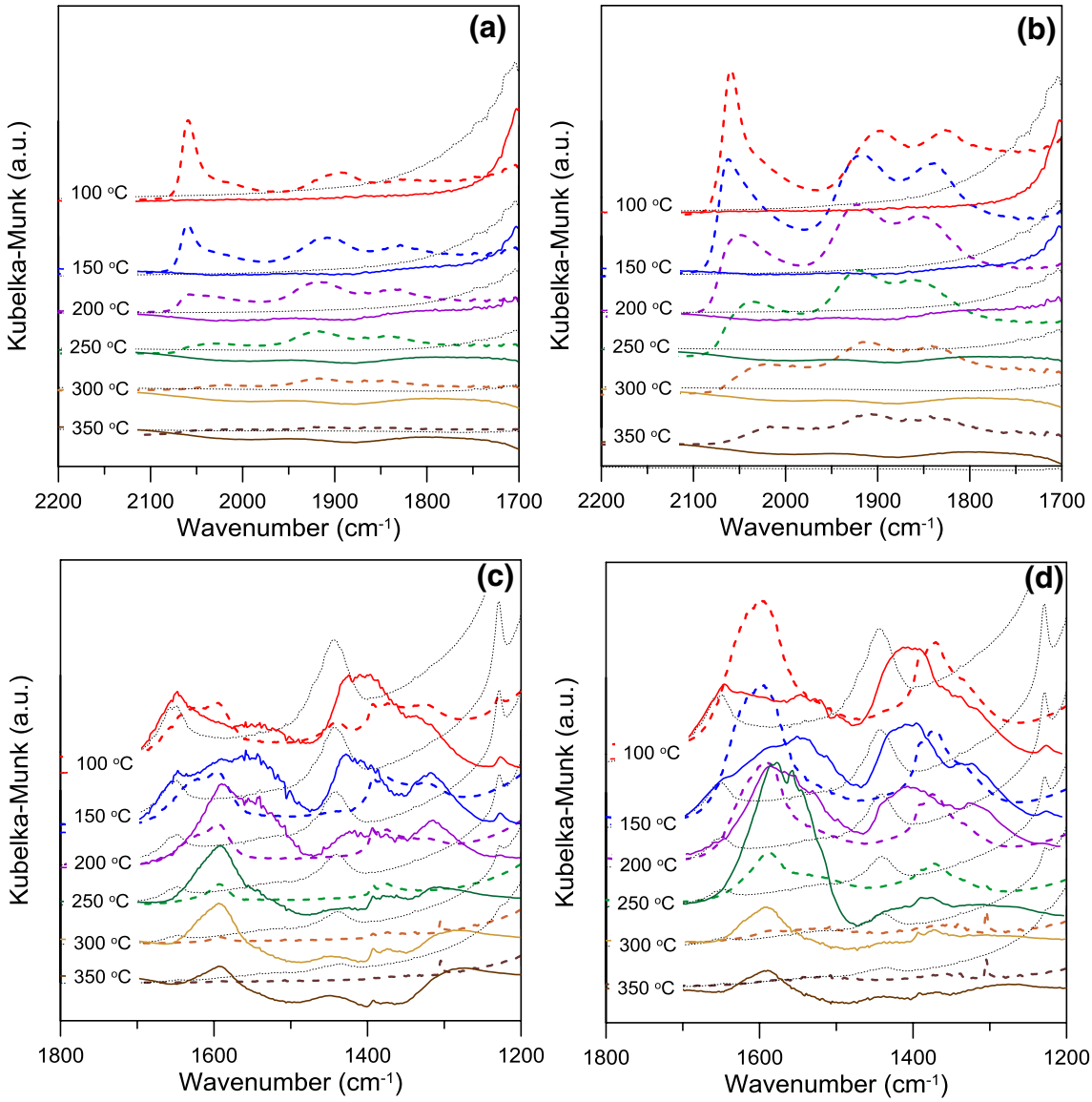

Fig. 7 DRIFTS spectra recorded at different temperatures in CO_2 methanation reaction performed in the presence of alumina support (dotted lines), Ni20–Al_2O_3 (**a, c**) and Ni20–Ce5–Al_2O_3 (**b, d**) catalysts after reduction (dashed lines) and after durability tests (solid lines) presented for selected regions 1700–2200 cm^{-1} (**a, b**) and 1200–1800 cm^{-1} (**c, d**)

spectra recorded in the CO_2 methanation reaction at 100 °C. Similar drop of the relative intensity as for Ni20–Al_2O_3 of on-top species and changes of positions of vibration bands of bridged carbonyls are observed with an increase in reaction temperature. The vibration bands of carbonyl groups are also not visible on the spectra recorded over promoted catalyst after durability test in the presence of H_2S. Therefore, one can assume that H_2S induces similar deactivation effects of the surface of promoted nickel catalyst.

Figure 7c, d show DRIFTS spectra in the region of 1200–1800 cm^{-1}, revealing formation of intermediate formate and carbonate species on the surface of alumina support, Ni20–Al_2O_3 and Ni20–Ce5–Al_2O_3 catalysts [59, 61, 63–67]. The vibration bands observed in the reaction over alumina support, located at around 1660, 1650, 1450 and 1230 cm^{-1}, can be ascribed to bicarbonates, whereas the vibrations observed at 1540 cm^{-1} may indicate the presence of monodentate carbonate. The intensity of corresponding groups gradually decreases with the increase in reaction temperature. Small maxima, which correspond to the presence of bicarbonates and carbonates can be detected on the spectra of Ni20–Al_2O_3 catalyst after high temperature reduction (see e.g. the bands at ca. 1440 and 1230 cm^{-1}), while their relative intensity is smaller on the spectra of promoted nickel catalyst. DRIFTS spectra of catalysts recorded at 100 °C reveal the presence of new bands in the region of 1500–1700 cm^{-1} and 1270–1420 cm^{-1}, which can be attributed to the formate species. Their relative intensity is higher in the promoted

catalyst. The enhancement of the formation of intermediate formate species may explain higher activity of cerium promoted catalysts. An increase in reaction temperature drives to the decrease of intensity of vibration bands. Weak vibration band located at around 1300 cm^{-1} appears on the spectra recorded above 200 °C. It can be attributed to the C–H vibrations in methane. In the case of spent catalysts the vibration bands of carbonates are also visible. Their position and intensity is slightly shifted in comparison to that on alumina. This effects can be in part related to the interaction of H_2S with CO_2 on the surface of alumina, resulted in the formation of thiocarbonates [61]. Slight maxima, which can be attributed to formates are also detectable on such catalysts, even in the reaction performed at 100 °C. Their higher intensity is visible for promoted catalyst. An increase in reaction temperature drives to the changes of intensity of carbonates and formates, however C–H vibrations, characteristic for methane are not detectable. Therefore, such effects may explain, why the catalysts in the final stage of durability tests in the presence of H_2S showed small activity, although the main reaction product was carbon monoxide, and higher CO_2 conversion was observed for promoted catalyst.

Carbon dioxide and hydrogen molecules, upon interaction with the surface of nickel crystallites may dissociate to form carbonyl groups (CO_{ad}), oxygen (O_{ad}) and hydrogen (H_{ad}) ad-atoms. In the following steps, in accordance to the "carbide mechanism", carbonyl groups can dissociate to oxygen (O_{ad}) and carbon (C_{ad}) surface ad-atoms, that are next converted to CH_x species or in accordance to other mechanism, may participate in the surface reactions with formation hydrogen-assisted intermediates, e.g. HCO and H_2CO species [68–70]. Therefore, strong adsorption of sulfur on the nickel sites may inhibit the initial stages of surface reaction and final hydrogenation of surface species. This mechanism explain also higher activity and longer operation time of the catalysts of larger number of active sites. Longer operation time of catalysts during durability tests in the presence of H_2S (presented in the Fig. 3) can be attributed to the higher active surface area of catalysts (Table 1). In turn, taking into account "associative reaction mechanism", the adsorption of carbon dioxide in the initial stages takes place on the specific surface sites located on the support or on the metal-support periphery region with subsequent formation of the appropriate carbonate-like or carbonyl species. Suitable intermediates can be subsequently hydrogenated to methane by the participation of hydrogen ad-atoms [71, 72]. Modification of the catalysts composition, e.g. by the changes of the acid-base properties or introduction of redox sites may induce changes of the interaction of CO_2 or intermediate species. Therefore, in accordance to this reaction mechanism, deactivation of nickel sites located in the close vicinity of the support, retardation of hydrogen activation and diffusion, as well as formation of some inactive species on the support due to the interaction with H_2S can be crucial for the course of the methanation reaction. Hence such changes may determine the operation time of catalysts. However, further detailed studies are needed to clarify these questions.

4 Conclusions

Alumina supported nickel catalysts, containing 20 and 40 wt% Ni were prepared by the impregnation method in the presence of citric acid. The catalysts were promoted with cerium. The catalysts showed high nickel dispersion. An increase in nickel content and introduction of promoter led to the increase of the active surface area. High activity of catalysts was observed at low reaction temperatures in CO_2 methanation reaction. Durability studies performed at high reaction temperature indicated high resistance of catalysts for sintering and coking. Electron scanning microscopy and Raman spectroscopy studies evidenced no formation of carbonaceous deposits. Durability tests performed in the presence of H_2S in CO_2–H_2 reaction mixture showed that the operation time of catalysts can be extended by the increase of active surface area of catalysts and the introduction Ce promoter. An in-situ DRIFTS studies of the fresh and spent catalysts indicated that deactivation of catalysts is connected with hindering of the initial stages of CO_2 methanation reaction, formation of surface carbonyl species and subsequent hydrogenation to methane. It was observed that the presence of Ce promoter may facilitate transformation of CO_2 molecules to the suitable intermediate species and change the course of deactivation of catalysts.

Acknowledgements Studies were carried out within ERA-NET Bioenergy project: "Development of an Innovative Concept for Carbon Dioxide Utilization as Side Stream of Integrated Bio-refinery Concepts" (ICOCAD), financed by National Centre for Research and Development (NCBR).

Open Access This article is distributed under the terms of the Creative Commons Attribution 4.0 International License (http://creativecommons.org/licenses/by/4.0/), which permits unrestricted use, distribution, and reproduction in any medium, provided you give appropriate credit to the original author(s) and the source, provide a link to the Creative Commons license, and indicate if changes were made.

References

1. A Roadmap for moving to a competitive low carbon economy in 2050, European Commission, Brussels, 8.3.2011 https://eur-lex.europa.eu/legal-content/EN/TXT/?uri=CELEX:52011DC0112
2. Climate Change 2013: The Physical Science Basis, Working Group I Contribution to the Fifth Assessment Report of the Intergovernmental Panel on Climate Change http://ipcc.ch/index.htm
3. Demirbas MF (2009) Appl. Energy. 86:S151–S161
4. Yang L, Ge X, Wan C, Yu F, Li Y (2014) Renew Sustain Energy Rev 40:133–1152

5. Naik SN, Goud VV, Rout PK, Dalai AK (2010) Sustain Energy Rev 14:578–597
6. Centi G, Quadrelli EA, Perathoner S (2013) Energy Environ Sci 6:1711–1731
7. Achinasa S, Achinasb V, Euverinka GJW (2017) Engineering 3:299–307
8. Kopyscinski J, Schildhauer TJ, Biollaz SMA (2010) Fuel 89:1763–1783
9. Aksoylu AE, Önsan ZI (1997) Appl Catal A: 164:1–11
10. Koschany F, Schlereth D, Hinrichsen O (2016) Appl Catal B 181:504–516
11. Aksoylu AE, Akin AN, Önsan ZI, Trimm DL (1996) Appl Catal 145:185–193
12. Hu CW, Yao J, Yang HQ, Chen Y, Tian AM (1997) J Catal 166:1–7
13. Garbarino G, Riani P, Magistri L, Busca G (2014) Int J Hydrogen Energy 39:11557–11565
14. Abello S, Berrueco C, Montane D (2013) Fuel 113:598–609
15. Lucchini MA, Testino A, Kambolis A, Proff C, Ludwig C (2016) Appl Catal B 182:94–101
16. Rombia E, Cutrufelloa MG, Atzoria L, Monacia R, Ardua A, Gazzolib D, Deianac P, Ferino I (2016) Appl Catal A 515:144–153
17. Graça I, González LV, Bacariza MC, Fernandes A, Henriques C, Lopes JM, Ribeiro MF (2014) Appl Catal B 147:101–110
18. Leitenburg C, Trovarelli A, Kašpar J (1997) J Catal 166:98–107
19. Ocampo F, Louis B, Kiwi-Minsker L, Roger AC (2011) Appl Catal A 392:36–44
20. Razzaq R, Zhu H, Jiang L, Muhammad U, Li C, Zhang S (2013) Ind Eng Chem Res 52:2247–2256
21. Razzaq R, Li C, Amin N, Zhang S, Suzuki K (2013) Energy Fuels 27:6955–6961
22. Pan Q, Peng J, Sun T, Gao D, Wang S, Wang S (2014) Fuel Process Technol 123:166–171
23. Cai M, Wen J, Chu W, Cheng X, Li Z (2011) J Nat Gas Chem 20:318–324
24. He L, Lin Q, Liu Y, Huang Y (2014) J Ener Chem 23:587–592
25. Abate S, Barbera K, Giglio E, Deorsola F, Bensaid S, Perathoner S, Pirone R, Centi G (2016) Ind Eng Chem Res 55:8299–8308
26. Abelló S, Berrueco C, Gispert-Guirado F, Montané D (2016) Catal Sci Technol 6:2305–23017
27. Gabrovska M, Edreva-Kardjieva R, Crisan D, Tzvetkov P, Shopska M (2012) Reac. Kinet. Mech Catal 105:79–99
28. Xu J, Froment GF (1989) AIChE J 35:88–96
29. Rahmani S, Rezaei M, Meshkani F (2014) J Ind Eng Chem 20:4176–4182
30. Qin Z, Ren J, Miao M, Li Z, Lin J, Xie K (2015) Appl Catal B 164:18–30
31. Liu H, Zou X, Wang X, Lu X, Ding W (2012) J Nat Gas Chem 21:703–707
32. Nie W, Zou X, Shang X, Wang X, Ding W, Lu X (2017) Fuel 202:135–143
33. Zhang L, Bian L, Zhu Z, Li Z (2018) Int J Hydrogen Energy 43:2197–2206
34. Michalska K, Kowalik P, Próchniak W, Borowiecki T (2018) Catal Lett 148:972–978
35. Garbarino G, Wang C, Cavattoni T, Finocchio E, Riani P, Flytzani-Stephanopoulos M, Busca G (2019) Appl Catal B 248:286–297
36. Rivero-Mendoza DE, Stanley JNG, Scott J, Aguey-Zinsou KF (2016) Catalysts 6:170
37. Wierzbicki D, Debek R, Motak M, Grzybek T, Gálvez ME, Da Costa P (2016) Catal Comm 83:5–8
38. Aksoylu AE, Isli AI, Önsan ZI (1999) Appl Catal A 183:357–364
39. Yan Y, Dai Y, He H, Yu Y, Yang Y (2016) Appl Catal B 196:108–116
40. Zhao K, Li Z, Bian L (2016) Front Chem Sci Eng 10:273–280
41. Hwang S, Hong UG, Lee J, Seo JG, Baik JH, Koh DJ, Lim H, Song IK (2013) J Ind Eng Chem 19:2016–2021
42. Pandey D, Deo G (2016) Chem Eng Commun 203:372–380
43. Tsuji M, Kodama T, Yoshida T, Kitayama Y, Tamaura Y (1996) J Catal 164:315–321
44. Broadbent HS, Slaugh LH, Jarvis NL (1954) J Am Chem Soc 76:1519–1523
45. Jiang M, Wang B, Yao Y, Wang H, Li Z, Ma X, Qin S, Sun Q (2013) Catal Commun 35:32–35
46. Liu J, Wang E, Lv J, Li Z, Wang B, Ma X, Qin S, Sun Q (2013) Fuel Process Technol 110:249–257
47. Appari S, Janardhanan VM, Bauri R, Jayanti S, Deutschmannd O (2014) Appl Catal A 471:118–125
48. Gac W, Zawadzki W, Słowik G, Sienkiewicz A, Kierys A (2018) Micropor Mesopor Mater 272:79–91
49. Gac W, Greluk M, Słowik G, Millot Y, Valentin L, Dzwigaj S (2018) Appl Catal B 237:94–109
50. Gao J, Wang Y, Ping Y, Hu D, Xu G, Gu F, Su F (2012) RSC Adv 2:2358–2368
51. Li C, Stair PC (1997) Catal Today 33:353–360
52. Wang Y, Alsmeyer DC, McCreery RL (1990) Chem Mater 2:557–563
53. Ferrari AC, Robertson (2000) J Phys Rev B 61:14095–14107
54. Cheng Z, Abernathy H, Liu M (2007) J Phys Chem C 111:17997–18000
55. Bartholomev CH (1987) Mechanism of nickel catalyst poisoning. In: Froment GF, Delmon B (eds) Catalyst deactivation. Elsevier Science Publisher B.V., Amsterdam, pp 81–104
56. Mare´cot P, Paraiso E, Dumas JM, Barbier J (1992) Appl Catal A 80:89–97
57. Hulteberg C (2012) Int J Hydrogen Energ 37:3978–3992
58. Argyle MD, Bartholomew CH (2015) Catalysts 5:145–269
59. Lamberti C, Zecchina A, Groppo E, Bordiga S (2010) Chem Soc Rev 39:4951–5001
60. Hadjiivanov K, Knözinger H, Mihaylov M (2002) J Phys Chem B 106:2618–2624
61. Davydov A (2003) Molecular spectroscopy of Oxide Catalyst surface Wiley, Chichester
62. Ozensoy E, Wayne Goodman D (2004) Phys Chem Chem Phys 6:3765–3778
63. Kubelkova' L, Nova´kova´ J, Jaeger NI, Schulz-Ekloff G (1993) Appl Catal A 95:87–101
64. Muroyama H, Tsuda Y, Asakoshi T, Masitah H, Okanishi T, Matsui T, Eguchi K (2016) J Catal 343:178–184
65. Wang X, Shi H, Kwak JH, Szanyi J (2015) ACS Catal 5:6337–6349
66. Peri J (1996) J Phys Chem 70:1482–1509
67. Morterra C, Magnacca G (1996) Catal Today 27:497–532
68. Andersson MP, Abild-Pedersen F, Remediakis IN, Bligaard T, Jones G, Engbæk J, Lytken O, Horch S, Nielsen JH, Sehested J, Rostrup-Nielsen JR, Nørskov JK, Chorkendorff I (2008) J Catal 255:6–19
69. Shetty S, Jansen APJ, van Santen RA (2009) J Am Chem Soc 131:12874–12875
70. Wind TL, Falsig H, Sehested J, Moses PG, Nguyen TTM (2016) J Catal 342:105–116
71. Panagiotopoulou P (2017) Appl Catal A 542:63–70
72. Aldana PAU, Ocampo F, Kobl K, Louis B, Thibault-Starzyk F, Daturi M, Bazin P, Thomas S, Roger AC (2013) Catal Today 215:201–207

Publisher's Note Springer Nature remains neutral with regard to jurisdictional claims in published maps and institutional affiliations.